



COMMUNICATIONS PHYSICS

ARTICLE

DOI: 10.1038/s42005-018-0083-7

OPEN

Topological photonic crystal nanocavity laser

Yasutomo Ota¹, Ryota Katsumi², Katsuyuki Watanabe¹, Satoshi Iwamoto^{1,2} & Yasuhiko Arakawa¹

Topological edge states exist at the interfaces between two topologically distinct materials. The presence and number of such modes are deterministically predicted from the bulk band topologies, known as the bulk-edge correspondence. This principle is highly useful for predictably controlling optical modes in resonators made of photonic crystals (PhCs), leading to the recent demonstrations of microscale topological lasers. Meanwhile, zero-dimensional topological trapped states in the nanoscale remained unexplored, despite its importance for enhancing light-matter interactions and for wide applications including single-mode nanolasers. Here, we report a topological PhC nanocavity with a near-diffraction-limited mode volume and its application to single-mode lasing. The topological origin of the nanocavity, formed at the interface between two topologically distinct PhCs, guarantees the existence of only one mode within its photonic bandgap. The observed lasing accompanies a high spontaneous emission coupling factor stemming from the nanoscale confinement. These results encompass a way to greatly downscale topological photonics.

¹Institute for Nano Quantum Information Electronics, The University of Tokyo, 4-6-1 Komaba, Meguro-ku, Tokyo 153-8505, Japan. ²Institute of Industrial Science, The University of Tokyo, 4-6-1 Komaba, Meguro-ku, Tokyo 153-8904, Japan. Correspondence and requests for materials should be addressed to Y.O. (email: ota@iis.u-tokyo.ac.jp)

The localization of waves in low dimensions constitutes a basis for diverse applications in various physical systems, including electron, sound and light. Given bulk band topologies, the bulk-edge correspondence, a physical principle that is originally developed for condensed matter physics¹, provides a deterministic route to localizing the waves: the difference in topological invariants between the two materials in contact is associated with the number of existing localized interface modes. Accordingly, zero-dimensional (0D) topological interface states², which function as cavities for the waves, can be defined a priori with knowing the bulk band topologies^{3–12}.

Regarding photonics, in which the control of the number of confined modes is vital for its applications, such deterministic design based on topology^{13–16} is highly desired. Indeed, the mode-number control in a micro/nanoscale cavity lacks a rigid strategy and still often relies on empirical approaches. This fact makes a stark contrast with the impressive progress in designing ultra-high Q factor and/or ultra-small mode volume (V) nanocavities based on photonic crystals (PhCs)^{17–19} and plasmonics²⁰. Recently, topological microcavity lasers designed based on the bulk-edge correspondence have been demonstrated^{4–6,21,22}. While the topological microcavities exhibited single-mode lasing,

the cavity designs do not totally deny the existence of other confined modes resonating near the lasing frequencies. Moreover, the spatial confinements of the microscale cavities are relatively weak, hampering the realization of strong light-matter interactions.

In this work, we report a topology-based, deterministic design of a single-mode PhC nanocavity and its application to lasing. We show that a 0D interface state is predictably formed between two PhC nanobeams with distinct Zak phases²³, topological invariants in the one-dimensional (1D) systems. The 0D edge state functions as a high Q factor nanocavity with a small V close to the diffraction limit²⁴. With semiconductor quantum dot gain, the nanocavity exhibits single-mode lasing with a high spontaneous emission coupling factor (β) of ~ 0.03 , which is orders of magnitude larger than those for conventional semiconductor lasers ($\beta \sim 10^{-6}$) and can be regarded as a hallmark consequence of the tight optical confinement^{25–28}.

Results

Design of a topological nanocavity. Figure 1a shows a design schematic of the topological PhC nanobeam cavity investigated in this study. Two airbridge PhC nanobeams^{19,28} respectively

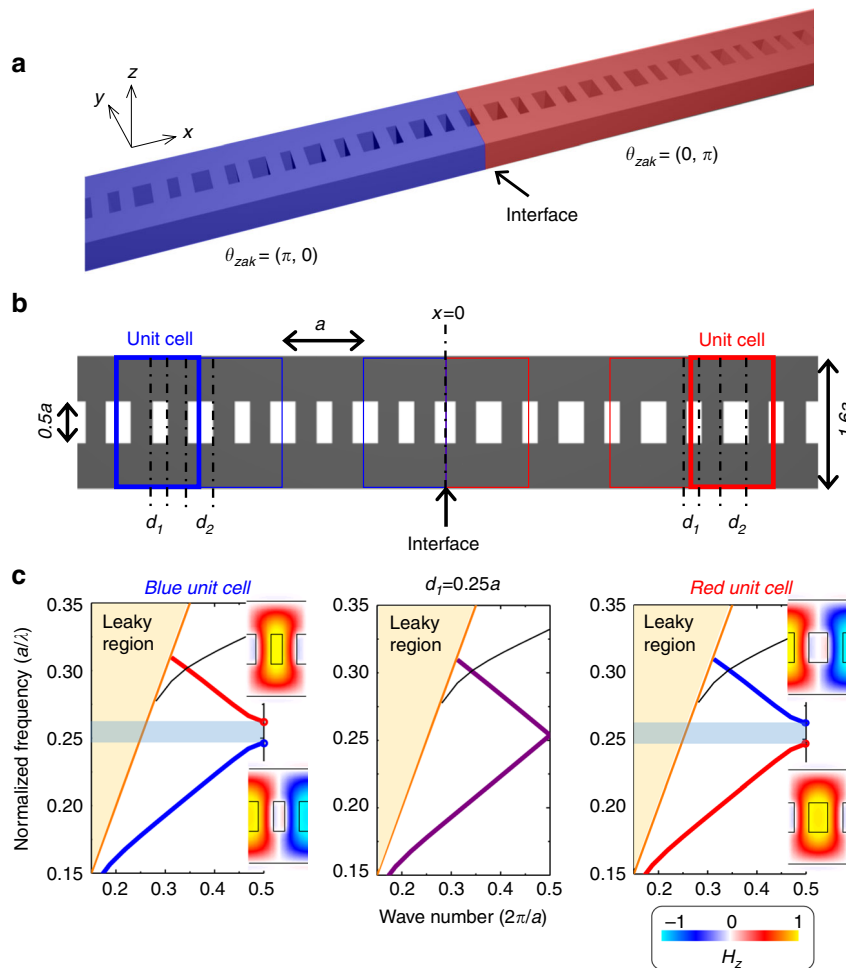


Fig. 1 Topological nanocavity design concept. **a** Schematic of the nanocavity formed by interfacing two photonic crystals (PhCs) with a common bandgap and distinct Zak phases. The Zak phases denoted in the bracket are respectively for the lowest and the second lowest band. **b** Detailed description of the design. The two PhCs are in essence the same but differ in the way that the unit cells are defined. Blue unit cell arranges the small airhole with a width of d_1 at the center, while red unit cell has the large airhole with d_2 at the center. The centers of the two holes respectively correspond to the inversion centers of the double periodic PhC. The sum of d_1 and d_2 equals to $0.5a$. **c** Band structures and wave functions at the band edges calculated for the PhC with the blue and red unit cell. The color of the band curve expresses its Zak phase (blue = π , red = 0). A band inversion occurs when swapping the unit cells. For the case of $d_1 = 0.25a$ ($= d_2$), a Dirac point appears at the band edge

colored in red and blue are interfaced at the cavity center. They share a common photonic band structure but are distinct in terms of the band topology characterized by the Zak phase, which is defined as an integral of the Berry connection over the first Brillouin zone²⁹. Further details of the design are found in Fig. 1b. The nanobeam is composed of GaAs-based unit cells (refractive index, $n = 3.4$) patterned with a period of a and is formed with a width of $1.6a$ and a thickness of $0.64a$, which are so small that the nanobeam supports a single transverse mode. The unit cells respectively contain two square-shape airholes with a width of $0.5a$, which are separated by half a period. The two airholes differ in their lengths, d_1 and d_2 , which relate each other via an equation $d_1 + d_2 = 0.5a$. The blue unit cell places the d_1 airhole at the center, while the red unit cell has the d_2 airhole at the center instead. In the following discussion, we consider situations with $d_1 \leq d_2$, such that $d_1 \leq 0.25a$. The two airholes are arranged within the unit cells so as to keep inversion symmetry, leading to the quantization of Zak phase to either 0 or π ²³. This allows for predicting the existence of an interface state solely based on the Zak phase²⁹, which is associated with the symmetry of the relevant bulk band wavefunction³⁰.

Figure 1c shows calculated 1D band structures using the three-dimensional (3D) plane wave expansion method for the blue and red unit cell when $d_1 = 0.19a$ (left and right panel, respectively) and $d_1 = 0.25a$ (center). At $d_1 = 0.25a$, the two airholes become identical and the nanobeam forms a gapless band structure with a Dirac point at the zone edge. Meanwhile, for $d_1 = 0.19a$, a photonic bandgap appears around a normalized frequency of $0.25a/\lambda$, where λ is the wavelength of light. The blue and red nanobeam share the same band structure, but the associated wave functions at the band edge have different parities: the blue (red) nanobeam supports a p (s)-wave-like magnetic mode with a function node at the unit cell center for the lowest band, while a

(p) -wave-like magnetic mode for the second lowest band. Since the optical mode at the zero frequency is always s -wave like, the lowest band for the blue unit cell should have a “twist” in its band nature somewhere in the momentum space. This makes the band topologically nontrivial in the sense of its finite Zak phase of π ³⁰, whereas the lowest band for the red unit cell can be regarded as topologically trivial.

Now, we consider a situation where the two 1D PhC nanobeams are put in contact as schematically shown in Fig. 1a, b. When considering the lowest-energy bandgap of the 1D system, there predictably exists a single 0D edge state at the interface, when and only when the interface is composed of two 1D PhCs with distinct Zak phases for the lowest bands²⁹. Suppose that only d_1 and d_2 vary in the system, the single modeness is robustly preserved as long as the two PhCs are topologically distinct, i.e., $d_1 \neq d_2$. The abrupt interface formed with the inversion-symmetric points eliminates the existence of other localized modes (Tamm modes) other than that of the topological origin (Shockley mode³⁰). In contrast, the conventional defect PhC nanocavities relying on index modulation sensitively vary the number of confined modes depending on the modulation pattern and in general cannot guarantee the single modeness^{19,28}. Further discussions on the existence of topological edge modes at a variety of interfaces composed of various 1D PhC nanobeams can be found in the supplementary material (see Supplementary Figures 1 and 2 and Supplementary Note 1).

We simulate the predicted interface modes of the designed nanobeams for different d_1 values by the 3D finite difference time domain method. Figure 2a shows the calculated electric field profiles of modes appear within the bandgaps. All the field distributions peak at the interfaces, with the field amplitude decreasing towards the exterior, demonstrating the existence of the localized cavity modes at the interfaces. We numerically

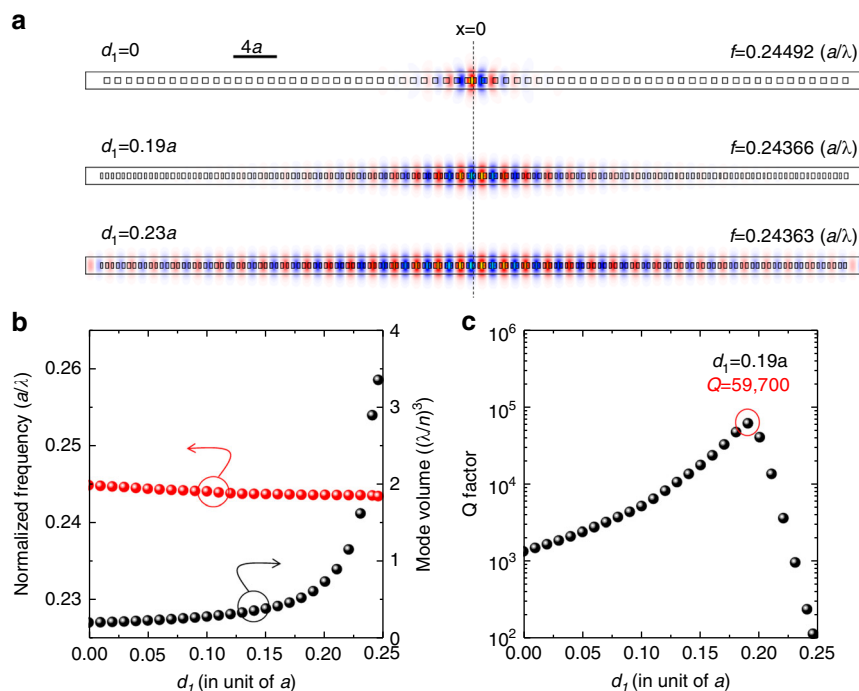


Fig. 2 Numerical simulation results. **a** Calculated electric (E_y) field profiles for the nanocavities with different d_1 values. A large modification in the mode extents as d_1 increases can be clearly seen. The f denotes the normalized frequency of the confined mode. **b** Simulated normalized frequencies (red) and mode volumes (black) plotted as a function of d_1 . The resonant frequencies are bound closely to the Dirac point, while the mode volumes vary largely as the photonic bandgap narrows by increasing d_1 . **c** Computed Q factors, showing a peak value of $\sim 60,000$ at $d_1 = 0.19a$. The quick decay of Q factor for $d_1 > 0.19a$ originates from the photon leakage from the finite-size simulation region, while the reduction for $d_1 < 0.19a$ is due to the light leakage into free space due to the tighter optical confinement

confirmed the existence of a single cavity mode within the bandgap of each structure through its excitation spectrum (see Supplementary Figure 2).

The spatial extent of the cavity mode depends largely on d_1 value, which essentially determines the depth and size of the corresponding bandgap and hence the optical penetration length into the PhC. In our design, the PhC with $d_1 = 0a$ possesses the largest bandgap and thus realizes the tightest optical confinement, resulting in a small mode volume of $0.23(\lambda/n)^3$, which is close to the conventional diffraction limit²⁴ of $\sim(\lambda/2n)^3$. This mode volume is at least an order of magnitude smaller than those reported in the previous topological microcavity designs^{4–6}. Figure 2b summarizes the evolution of V_s when increasing d_1 , showing an exponential-like increase. Meanwhile, interestingly, the calculated resonant frequencies, shown as the red balls in the same plot, do not exhibit a significant dependence on d_1 ³¹.

In addition, we calculated the Q factors of the edge modes for different d_1 values and plotted them in Fig. 2c. The Q factor peaks at $d_1 = 0.19a$ and decreases for both higher and lower d_1 values. For $d_1 \sim 0a$, the optical confinement is too strong to suppress leaky components violating the condition for the total internal reflection, resulting in low Q factors of only about 1000. When increasing d_1 from $0a$, the Q factor improves at the expense of enlarged mode volume. For $d_1 > 0.2a$, Q factor rapidly degrades since the mode size becomes so large compared to that of the allocated simulation domain (70 periods in the x direction), which leads to the light leakage through the domain boundaries. Interestingly, the existence of the 0D edge mode is robust: it resonates even when the patterned PhC area is harshly reduced to containing only a few unit cells³¹. In the current design and simulation size, at $d_1 = 0.19a$, the topological nanocavity support the maximum Q factor of 59,700 with a mode volume of $0.67(\lambda/n)^3$, which are comparable to those for existing PhC nanobeam cavities employed for laser application²⁸. The topology-based design enables the wide control of Q factor and mode volume while strictly keeping the single modeness of the nanocavity. This property is highly beneficial to develop single-mode lasers using broadband gain media, including semiconductor quantum dots, since such inhomogeneously broadened gain media often hamper the selection of a single lasing mode by controlling gain properties.

Sample fabrication and optical characterization. We fabricated the designed topological nanocavities with $a = 270$ nm into a 180 nm-thick GaAs slab containing InAs quantum dots (see Methods) using standard semiconductor nanofabrication processes. The total length of the nanobeam was set to 20 μm (including 68 unit cells). A scanning electron microscope image of a nanocavity designed with $d_1 = 0.19a$ is shown in Fig. 3a. Unlike the theoretical model, the airholes are not perfect squares and possess rounded edges. In the topology-based design, however, the hole shape does not critically influence the existence of the cavity mode as far as the topological bandgap remains opened.

To characterize the fabricated nanocavity, we performed micro-photoluminescence (μPL) measurements at a low temperature of 10 K (see Methods). We used a modulated diode laser oscillating at 808 nm (repetition rate 5 MHz, pulse width 20 ns) and an objective lens for the optical pump of the samples. PL signals were analyzed with a grating spectrometer and an InGaAs camera. Figure 3b–d shows a series of PL spectra measured with an average pump power of 2.3 μW for the nanocavities designed using different d_1 s of $0a$, $0.19a$ and $0.23a$. Each spectrum exhibits a single strong peak resonating around a common wavelength of ~ 1040 nm, as indicated by a colored arrow in the figure. The peak arises from the designed edge mode localized at the interface,

confirmed through the experimental evidences provided below. In the figure, we also plotted PL spectra measured for homogeneous PhC nanobeams without the topological interfaces using gray solid lines. The spectra show the frequencies of the band edges of the respective designs (indicated by gray arrows). As expected from the design principle, the bandgaps that span between the pairs of the band edge peaks actually enclose the emission peaks originated from the interfaces. The measured peak frequencies of the emission peaks are summarized in Fig. 3e. All the peak positions agree well with those simulated using the plane wave expansion method (solid lines). A highlight of the plot is the nearly fixed resonant frequencies of the in-gap mode, which are in line with the predicted behavior of the topological edge states. Then, we investigate the spatial extents of the edge modes by measuring the pump position dependences of the PL spectra. The pump spot size in this experiment was about 2 μm . Figure 3f shows the normalized peak intensities of the interface modes taken along the x direction. The three curves are of the nanocavities with different d_1 s and clearly exhibit the mode sizes being dependent on d_1 . The case of $d_1 = 0a$ and $d_1 = 0.23a$ respectively show the smallest and largest mode distribution, as expected from the simulations. We note that the measured intensity profiles compare well with those simulated, after taking into account the spatial resolution of our measurement setup (see Supplementary Figure 3 and Supplementary Note 2). For detailed characterization of the field profiles, it will be important to directly evaluate them using, e.g., scanning near-field optical microscopes³². We also characterized the Q factors of the interface modes of different d_1 s and the corresponding PL spectra are depicted in the insets in Fig. 3b–d. The Q factors for $d_1 = 0a$ and $d_1 = 0.23a$ are measured to be only 700 and 600, respectively. In contrast, we observed a high Q factor of at least over 2000 for $d_1 = 0.19a$. The measured Q factor for the nanocavity of $d_1 = 0.19a$ is limited by the spectrometer resolution (~ 400 μeV) used in this particular measurement as well as by the absorption originated from the embedded quantum dots. Therefore, its precise characterization requires further measurements, which we will discuss in the following.

Now, we study the pump power dependence of the topological edge state formed in the $d_1 = 0.19a$ nanocavity, in order to verify its lasing oscillation using the quantum dot gain. For the measurements, we reduced the repetition rate of the pump pulses to 0.5 MHz. Figure 4a displays two spectra taken with respective peak pump powers of 5 μW and 150 μW . For the low pump power PL spectrum, we observe broad background emission stemming from the quantum dot spontaneous emission, together with a sharp peak of the localized cavity mode. It is apparent that, with increasing the pump power, the cavity mode emission grows dramatically and dominates the spectrum. In Fig. 4b, c, we summarize the peak integrated intensities of the cavity mode measured under various pump powers. The light-in-light-out curve indeed exhibits an intensity jump giving a s -like shape, which is typical for lasers and is well fitted using a semiconductor laser model^{26,33} (see Methods). Through the fit, we deduce a peak threshold pump power of 46 μW and a spontaneous emission coupling factor (β) of 0.03 for this laser: this high β value, which is orders of magnitude larger than those for conventional semiconductor lasers, can be read as a hallmark of nanolasers with tight optical confinement^{25–28}. Nevertheless, the estimated β is relatively smaller than those reported for similar PhC nanolasers²⁸. We consider that this arises from the use of the excited state of the quantum dots (QDs) for the laser gain, where fast non-radiative carrier recombination processes may reduce β in appearance^{28,33} (see also Methods). In Fig. 4c, concomitant to the sharp intensity increase, we observed a clamp of the background emission (see green points), as another expected

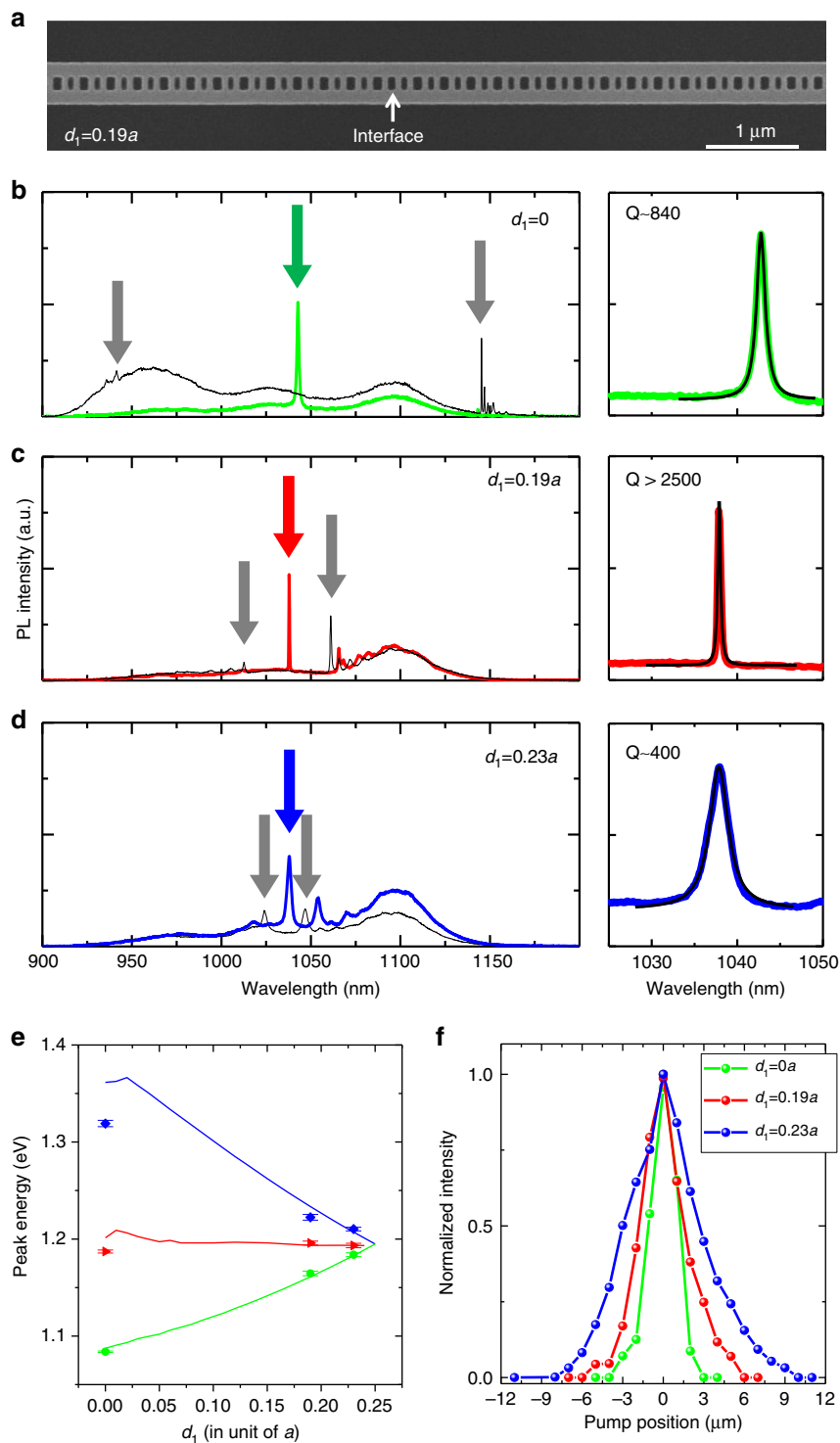


Fig. 3 Basic experimental characterization of the topological nanocavities. **a** Scanning electron microscope image of a fabricated nanocavity with $d_1 = 0.19a$. **b-d** Measured photoluminescence (PL) spectra for the fabricated photonic crystal (PhC) nanobeams with different d_1 values. The colored curves are of topologically nontrivial interfaces, while the black curves are of regular PhCs. Arrows indicate the spectral peak positions of the topological zero-dimensional (OD) edge modes (colored) and of the band edges (gray). The band edge positions are determined by the two closest neighbor peaks from the cavity peak. Each right inset shows a close up spectrum of the topological edge state. The black curves overlaid on the graphs are fitting. **e** Summary of the measured peak positions plotted as a function of d_1 . The magenta data points are of the OD confined modes, while the brown (dark green) data points are of the higher (lower) energy band edges. The error bar for each point expresses the standard deviation deduced from the measurement on 10 samples with the same design. The solid lines show simulated peak positions by the three-dimensional plane wave expansion method. The simulated curves are plotted with a constant offset for better comparison with the experimental results. **f** Position-dependent PL intensities measured for the topological nanocavities with different d_1 values. Tighter mode localization for smaller d_1 , as expected from the numerical modeling, is demonstrated

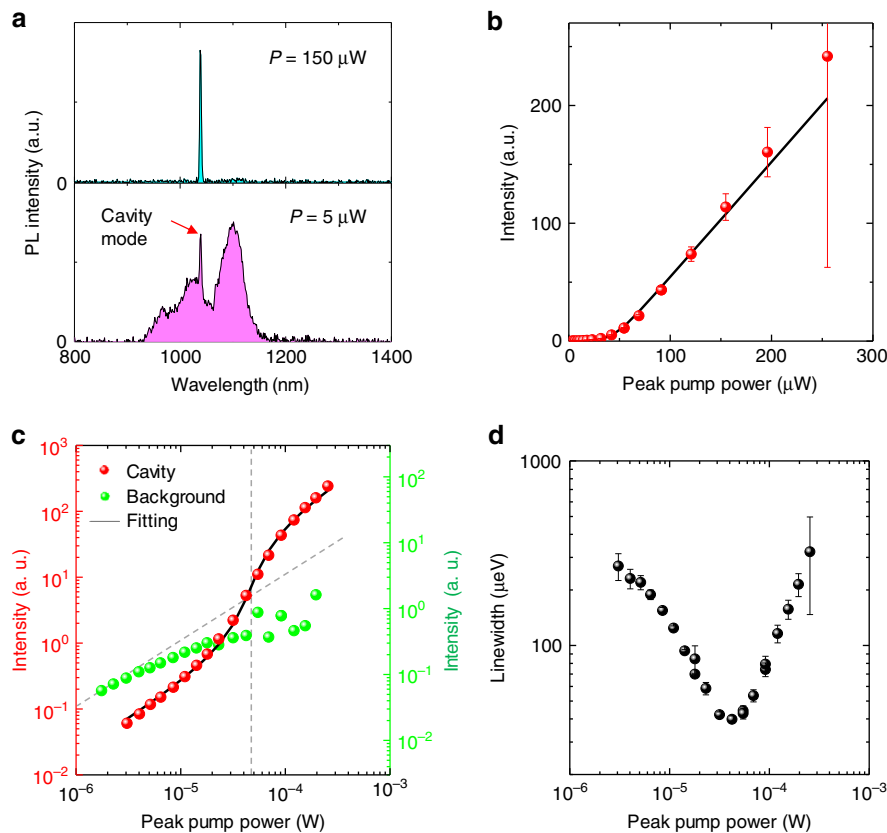


Fig. 4 Laser oscillation from the topological nanocavity designed with $d_1 = 0.19a$. **a** Photoluminescence (PL) spectra measured with two different peak pump powers. For the low pumping power of $5 \mu\text{W}$, broad background emission from the quantum dots (QDs), spanning from $\sim 900 \text{ nm}$ to 1200 nm , dominates the spectrum. For the higher pumping power, the background is suppressed and the cavity emission peak in turn prevails. **b** Light-in-light-out (LL) plot for the emission peak of the zero-dimensional (0D) edge state. The black solid line is the fitting to the data points. Laser transition with a threshold peak pump power of $46 \mu\text{W}$ is seen. Error bars express standard errors deduced by fitting. **c** Logarithmic plots of the LL curve (red) and of the evolution of the intensities of the background emission (light green). The LL curve exhibits a mild S-shaped curve, which is typical for high- β lasers. The vertical dashed line indicates the threshold pump power. The background emission clamps above the laser threshold. The diagonal dashed line is an eye guide with a linear increase. The scattered data points above the threshold originate from the noisy PL spectra for the QD emission, due to strong cavity emission and the limited dynamic range of our detector. **d** Measured evolution of cavity linewidths as a function of peak pump power. The linewidths were extracted by fitting to the high resolution spectra with Lorentzian peak functions convolved with a Gaussian function representing the spectrometer response ($\sim 40 \mu\text{eV}$). Linewidths shows a significant narrowing of nearly an order of magnitude. The increase of the linewidth above the lasing threshold is likely due to heating in the nanocavity. Error bars express standard errors deduced by fitting

phenomenon for lasing. Figure 4d shows the evolution of the measured cavity linewidths as a function of pump power, evaluated by using a higher-resolution spectrometer. A significant linewidth narrowing by nearly an order of magnitude is observed, further confirming the lasing oscillation in the investigated topological nanocavity. At a transparency pump power of $11 \mu\text{W}$ (estimated from the laser model used for the fitting), we estimated a cold cavity Q factor of ~ 9600 , experimentally demonstrating the formation of a high Q factor mode by the topology-based design. The current limiting factor of the achievable Q factor would be fabrication imperfection, since the current topological design requires smaller airhole sizes than those of conventional PhC defect-cavity designs resonating at the same wavelength²⁸. It is noteworthy that the observed lasing can be regarded as quasi-continuous wave since all the dynamics within the laser are much faster than the pump pulse duration.

Discussion

In the current work, we have demonstrated single-mode lasing using a topological nanocavity with QD gain. At the design level, the single modeness of the nanocavity within the corresponding

bandgap is guaranteed as far as the bandgap remains opened, thanks to the topological protection associated with the bulk-edge correspondence. Experimentally, even under harsh pumping to the system, the topological cavity mode will be sustained unless the pumping becomes stronger than that closing the bulk bandgap. Meanwhile, there are some possibilities of emerging confined modes due to focused optical pumping. Such carrier injection locally modifies the refractive index of the host material, which may lead to the formation of cavity modes within the mode gaps³⁴. However, we did not observe the rise of such modes in the current experimental conditions. This would be due to very-low refractive index change in the current carrier pumping conditions. The low refractive index change is indirectly confirmed via the marginal change in the laser wavelengths during measuring pump power dependence (see Supplementary Figure 4 and Supplementary Note 3). Additionally, we note that we did not observe lasing when using the same 1D nanobeams without the topological interfaces. As seen in Fig. 3b–d, they support band edge modes, the Q factors of which, however, are too low to achieve lasing with the gain of our QDs. We note that the suppression of lasing from such band edge mode is easy, since they spread the entire PhC and thus their Q factors rapidly degrades

by reducing the number of periods of the PhC. Overall, all these properties facilitate the robustness of single-mode lasing in our topological nanocavity.

In addition, the robust single-mode lasing observed in the current work infers that gain/loss and optical nonlinearities accompanied with optical pumping have only a minor influence on the properties of the topological nanocavity. This is largely due to the weak pumping powers in the current experiments, which is confirmed via the marginal changes of cavity resonant wavelengths. Meanwhile, for future studies, it will be of great interest to investigate the nature of topological edge states under the presence of strong gain and loss^{35–37}. The influence of nonlinearities on the characteristics of topological PhC lasers^{38–40} will also be of importance from a perspective of practical applications.

In summary, we realized a topological PhC nanocavity laser. We employed the bulk-edge correspondence to deterministically define single-mode PhC nanocavities, which support high Q factors and small mode volumes, both of which were confirmed theoretically and experimentally. The tight optical confinement effect manifested itself as the observed high- β lasing. Our results showcase an example on how topological physics penetrates into nanophotonics and on how to downscale topological photonics into the nanoscale. We believe that topological photonics^{15,16} will renew and advance the understanding and the engineering of nanoscale resonators and lasers.

Methods

QD wafer used for sample fabrication. We fabricated the designed topological nanocavities into a 180 nm-thick GaAs slab. The slab is grown by molecular beam epitaxy and contains 5 layers of InAs QDs with an areal density of $3.6 \times 10^{10} \text{ cm}^{-2}$ per layer. At 10 K, the ground state emission of the QD ensemble is peaked at $\sim 1100 \text{ nm}$ with a spectral full width half maximum of 45 meV. Under strong optical pumping, the QD ensemble exhibits spectrally broad PL emission with additional two peaks associated with the excited state emission at $\sim 1030 \text{ nm}$ (the first excited state) and at $\sim 970 \text{ nm}$ (the second excited state).

Laser model used for fitting of the measured light output curve. We fitted the measured light output curve shown in Fig. 4b, c using a conventional semiconductor laser model³³ described below.

$$\frac{dn}{dt} = -kn + \beta\gamma(N - N_t)n + \beta\gamma N,$$

$$\frac{dN}{dt} = P - \gamma N - \beta\gamma(N - N_t)n,$$

where n and N are the cavity photon and carrier number, respectively. N_t is the transparent carrier number and estimated to be 3500. κ is the transparent cavity leakage rate of $125 \mu\text{eV}$; γ is the total spontaneous emission rate of $0.66 \mu\text{eV}$; P is the pump power; and β describes the spontaneous emission coupling factor and is treated as a main fitting parameter. Since the pump duration (20 ns) is much longer than all the laser dynamics, the laser is assumed to be operated under continuous wave pumping. As such, we can set $dt = 0$. The kn corresponds to light output intensity, which is to be fitted with the experimental output curve. Using a non-linear least squared method, we found the best fitting when $\beta = 0.03$. Here, we did not take into account non-radiative carrier recombination processes, which are known to reduce β value in appearance: i.e., the non-radiative processes result in a larger intensity jump in the output curve across the threshold, which can be interpreted as a reduction of β when not considering the non-radiative processes. Accordingly, the estimated β of 0.03 can be regarded as the lowest bound for the current laser device.

Optical measurement setup. Figure 5 shows a schematic of the μPL setup used for the experiments. The fabricated samples are located within the cryostat cooled with liquid helium. The cryostat is placed on a stepping motor for course positioning and on piezo stages for fine adjustment as well. We access each sample with an objective lens with a magnification of 50. By inserting a beam splitter, we introduce excitation laser beam focused on the sample. The diameter of the focusing spot was estimated to be $\sim 2 \mu\text{m}$, relating a peak pump power of $1 \mu\text{W}$ to a pump density of $\sim 30 \text{ W cm}^{-2}$. The PL signal is collected by the same lens and sent to a spectrometer equipped with a cooled InGaAs camera. The spectrometer resolution can be switched by changing diffraction gratings. In the detection optical path, we inserted a long-wavelength-path filter in order to reject the pump laser beam oscillating at a wavelength of 808 nm. The entrance slit of the spectrometer is

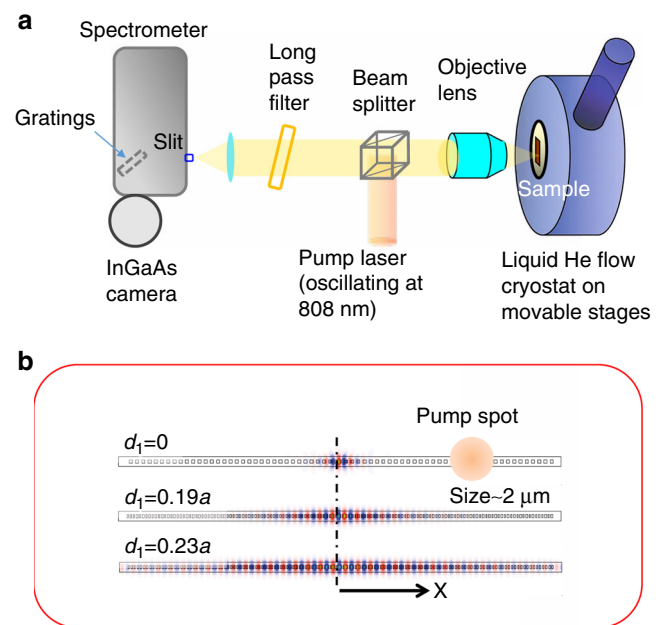


Fig. 5 Optical measurement setup. **a** Schematic illustration. **b** Relationship between the PhC nanobeam and the laser spot (which corresponds to the detection position). The simulated field distributions of the topological cavity modes are overlaid

narrowed down to $\sim 50 \mu\text{m}$, allowing for spatial filtering with a width of $\sim 2 \mu\text{m}$ along with the nanobeam. The optical path is aligned so that PL signal at the pump position is guided into the spectrometer. For performing the position-dependent PL measurements, we solely shifted the sample position with respect to the x -axis using the piezo stage. The relationship between the pump and detection position is fixed during the measurements. The spatial resolution of this measurement is roughly assumed to be $2 \mu\text{m}$.

Data availability

The data that support the findings of this study are available from the corresponding author upon reasonable request.

Received: 12 July 2018 Accepted: 26 October 2018

Published online: 22 November 2018

References

- Hatsugai, Y. Chern number and edge states in the integer quantum Hall effect. *Phys. Rev. Lett.* **71**, 3697–3700 (1993).
- Su, W. P., Schrieffer, J. R. & Heeger, A. J. Solitons in polyacetylene. *Phys. Rev. Lett.* **42**, 1698–1701 (1979).
- Gao, W. S., Xiao, M., Chan, C. T. & Tam, W. Y. Determination of Zak phase by reflection phase in 1D photonic crystals. *Opt. Lett.* **40**, 5259 (2015).
- St-Jean, P. et al. Lasing in topological edge states of a one-dimensional lattice. *Nat. Photonics* **11**, 651–656 (2017).
- Zhao, H. et al. Topological hybrid silicon microlasers. *Nat. Commun.* **9**, 981 (2018).
- Parto, M. et al. Edge-mode lasing in 1D topological active arrays. *Phys. Rev. Lett.* **120**, 113901 (2018).
- Tan, W., Sun, Y., Chen, H. & Shen, S.-Q. Photonic simulation of topological excitations in metamaterials. *Sci. Rep.* **4**, 3842 (2015).
- Poli, C., Bellec, M., Kuhl, U., Mortessagne, F. & Schomerus, H. Selective enhancement of topologically induced interface states in a dielectric resonator chain. *Nat. Commun.* **6**, 6710 (2015).
- Slobozhanyuk, A. P., Poddubny, A. N., Miroshnichenko, A. E., Belov, P. A. & Kivshar, Y. S. Subwavelength topological edge states in optically resonant dielectric structures. *Phys. Rev. Lett.* **114**, 123901 (2015).
- Xiao, M. et al. Geometric phase and band inversion in periodic acoustic systems. *Nat. Phys.* **11**, 240–244 (2015).
- Xiao, Y.-X., Ma, G., Zhang, Z.-Q. & Chan, C. T. Topological subspace-induced bound state in the continuum. *Phys. Rev. Lett.* **118**, 166803 (2017).

12. Kim, I., Iwamoto, S. & Arakawa, Y. Topologically protected elastic waves in one-dimensional phononic crystals of continuous media. *Appl. Phys. Express* **11**, 017201 (2018).
13. Haldane, F. D. M. & Raghu, S. Possible realization of directional optical waveguides in photonic crystals with broken time-reversal symmetry. *Phys. Rev. Lett.* **100**, 013904 (2008).
14. Wang, Z., Chong, Y., Joannopoulos, J. D. & Soljačić, M. Observation of unidirectional backscattering-immune topological electromagnetic states. *Nature* **461**, 772–775 (2009).
15. Lu, L., Joannopoulos, J. D. & Soljačić, M. Topological photonics. *Nat. Photonics* **8**, 821–829 (2014).
16. Ozawa, T. et al. Topological photonics. *arXiv* **1802**, 04173 (2018).
17. Asano, T., Ochi, Y., Takahashi, Y., Kishimoto, K. & Noda, S. Photonic crystal nanocavity with a Q factor exceeding eleven million. *Opt. Express* **25**, 1769 (2017).
18. Hu, S. et al. Experimental realization of deep subwavelength confinement in dielectric optical resonators. *arXiv* **1707**, 04672 (2017).
19. Deotare, P. B., McCutcheon, M. W., Frank, I. W., Khan, M. & Lončar, M. High quality factor photonic crystal nanobeam cavities. *Appl. Phys. Lett.* **94**, 121106 (2009).
20. Oulton, R. F. et al. Plasmon lasers at deep subwavelength scale. *Nature* **461**, 629–632 (2009).
21. Bahari, B. et al. Nonreciprocal lasing in topological cavities of arbitrary geometries. *Science* **358**, 636–640 (2017).
22. Bandres, M. A. et al. Topological insulator laser: experiments. *Science* **359**, eaar4005 (2018).
23. Zak, J. Berry's phase for energy bands in solids. *Phys. Rev. Lett.* **62**, 2747–2750 (1989).
24. Boroditsky, M., Coccioli, R., Yablonovitch, E., Rahmat-Samii, Y. & Kim, K. W. Smallest possible electromagnetic mode volume in a dielectric cavity. *IEE Proc. Optoelectron* **145**, 391–397 (1998).
25. Khajavikhan, M. et al. Thresholdless nanoscale coaxial lasers. *Nature* **482**, 204–207 (2012).
26. Ota, Y., Kakuda, M., Watanabe, K., Iwamoto, S. & Arakawa, Y. Thresholdless quantum dot nanolaser. *Opt. Express* **25**, 19981 (2017).
27. Takiguchi, M. et al. Systematic study of thresholdless oscillation in high- β buried multiple-quantum-well photonic crystal nanocavity lasers. *Opt. Express* **24**, 3441 (2016).
28. Zhang, Y. et al. Photonic crystal nanobeam lasers. *Appl. Phys. Lett.* **97**, 051104 (2010).
29. Xiao, M., Zhang, Z. Q. & Chan, C. T. Surface impedance and bulk band geometric phases in one-dimensional systems. *Phys. Rev. X* **4**, 021017 (2014).
30. Zak, J. Symmetry criterion for surface states in solids. *Phys. Rev. B* **32**, 2218–2226 (1985).
31. Kalozoumis, P. A. et al. Finite size effects on topological interface states in one-dimensional scattering systems. *arXiv* **1712**, 08763 (2017).
32. Lalouat, L. et al. Subwavelength imaging of light confinement in high-Q/small-V photonic crystal nanocavity. *Appl. Phys. Lett.* **92**, 111111 (2008).
33. Bjork, G. & Yamamoto, Y. Analysis of semiconductor microcavity lasers using rate equations. *IEEE J. Quantum Electron.* **27**, 2386–2396 (1991).
34. Notomi, M. & Taniyama, H. On-demand ultrahigh-Q cavity formation and photon pinning via dynamic waveguide tuning. *Opt. Express* **16**, 18657 (2008).
35. Schomerus, H. Topologically protected midgap states in complex photonic lattices. *Opt. Lett.* **38**, 1912 (2013).
36. Malzard, S., Poli, C. & Schomerus, H. Topologically protected defect states in open photonic systems with non-hermitian charge-conjugation and parity-time symmetry. *Phys. Rev. Lett.* **115**, 200402 (2015).
37. Leykam, D., Bliokh, K. Y., Huang, C., Chong, Y. D. & Nori, F. Edge modes, degeneracies, and topological numbers in non-Hermitian systems. *Phys. Rev. Lett.* **118**, 28–30 (2017).
38. Harari, G. et al. Topological insulator laser: theory. *Science* **359**, eaar4003 (2018).
39. Malzard, S. & Schomerus, H. Nonlinear mode competition and symmetry-protected power oscillations in topological lasers. *New J. Phys.* **20**, 063044 (2018).
40. Longhi, S., Kominis, Y. & Kovanis, V. Presence of temporal dynamical instabilities in topological insulator lasers. *Europhys. Lett.* **122**, 14004 (2018).

Acknowledgements

The authors thank Y. Hatsugai, C.F. Fong and I. Kim for fruitful discussions. This work was supported by JSPS KAKENHI Grant-in-Aid for Specially promoted Research (15H05700), KAKENHI(17H06138, 15H05868) and JST-CREST and was based on results obtained from a project commissioned by the New Energy and Industrial Technology Development Organization (NEDO).

Author contributions

Y.O. and S.I. designed the topological nanocavity with the assistance of R.K. Y.O. performed the optical characterization of the nanocavities fabricated by R.K. Y.O. analyzed the data and wrote the manuscript with input from all the authors. K.W. grew the QD wafer. S.I. and Y.A. supervised the project.

Additional information

Supplementary information accompanies this paper at <https://doi.org/10.1038/s42005-018-0083-7>.

Competing interests: The authors declare no competing interests.

Reprints and permission information is available online at <http://npg.nature.com/reprintsandpermissions/>

Publisher's note: Springer Nature remains neutral with regard to jurisdictional claims in published maps and institutional affiliations.



Open Access This article is licensed under a Creative Commons Attribution 4.0 International License, which permits use, sharing, adaptation, distribution and reproduction in any medium or format, as long as you give appropriate credit to the original author(s) and the source, provide a link to the Creative Commons license, and indicate if changes were made. The images or other third party material in this article are included in the article's Creative Commons license, unless indicated otherwise in a credit line to the material. If material is not included in the article's Creative Commons license and your intended use is not permitted by statutory regulation or exceeds the permitted use, you will need to obtain permission directly from the copyright holder. To view a copy of this license, visit <http://creativecommons.org/licenses/by/4.0/>.

© The Author(s) 2018